

Optical creation of a supercrystal with three-dimensional nanoscale periodicity

V. A. Stoica¹, N. Laanait², C. Dai¹, Z. Hong¹, Y. Yuan¹, Z. Zhang³, S. Lei¹, M. R. McCarter⁴, A. Yadav⁴, A. R. Damodaran⁴, S. Das⁴, G. A. Stone¹, J. Karapetrova³, D. A. Walko³, X. Zhang³, L. W. Martin^{4,5}, R. Ramesh^{4,5}, L.-Q. Chen¹, H. Wen³, V. Gopalan^{1*} and J. W. Freeland^{3*}

Stimulation with ultrafast light pulses can realize and manipulate states of matter with emergent structural, electronic and magnetic phenomena. However, these non-equilibrium phases are often transient and the challenge is to stabilize them as persistent states. Here, we show that atomic-scale PbTiO₃/SrTiO₃ superlattices, counterpoising strain and polarization states in alternate layers, are converted by sub-picosecond optical pulses to a supercrystal phase. This phase persists indefinitely under ambient conditions, has not been created via equilibrium routes, and can be erased by heating. X-ray scattering and microscopy show this unusual phase consists of a coherent three-dimensional structure with polar, strain and charge-ordering periodicities of up to 30 nm. By adjusting only dielectric properties, the phase-field model describes this emergent phase as a photo-induced charge-stabilized supercrystal formed from a two-phase equilibrium state. Our results demonstrate opportunities for light-activated pathways to thermally inaccessible and emergent metastable states.

The structural and functional complexity of artificial nanomaterials challenges the frontiers of experimental capability, calling for novel approaches to materials synthesis. During the past few decades, a new class of ‘non-equilibrium photo-induced materials’, which exist only in the transient state, has emerged under ultrafast-optical excitation. Although, in the vast majority of cases, either electronic, magnetic, or structural orders undergo prompt collapse into disorder^{1–3}, in a few other cases, novel orders have been stabilized, such as a switch of the order parameter in the magnetic compounds⁴ and the creation of new condensates such as superconductors⁵, charge/spin density waves^{6,7} and amorphous-to-crystalline transformations⁸. More recently, new phases not present in an equilibrium thermodynamic phase diagram have arisen out of the non-equilibrium optical excitation either as transient^{9,10} or persistent^{11,12} states. Such thermally inaccessible states are both of fundamental interest, as they offer a unique window into a regime of strong coupling between microscopic degrees of freedom in a material, and could possess novel functionalities not present in equilibrium states. However, irrespective of the physical nature of the excited state or the equilibrium parent phase, a key challenge remains: namely, the conversion of the transient states into new persistent phases at room temperature.

A central idea exploited in this work is to counterpoise distinct order parameters in an atomic-scale heterostructure so as to produce a ground state that is very susceptible to external perturbations, such as fields and light. In particular, we explore (PbTiO₃)_n/(SrTiO₃)_n superlattices (PTO/STO superlattices), where there is a subtle balance between the polarization (Landau), electric, gradient and elastic energies. The energetics of these heterostructures is dictated by interlayer coupling through electrostatic as well as elastic strain gradients, producing confinement and proximity of competing phases^{13–17}. When this system is grown on DyScO₃ (DSO)

substrates, the SrTiO₃ is under tensile strain, which induces an in-plane polarization, and PbTiO₃ is under compression, which favours out-of-plane polarization. However, this leads to highly charged interfaces; to avoid it, the system devolves into a two-phase mixture of ferroelectric–ferroelastic a_1/a_2 domains (FE) and polarization vortices (V) in the as-grown samples^{15,16}.

Starting from this two-phase mixture, here we show that by using an ultrafast optical pulse, we can manipulate the electrostatic landscape and enable the formation of a stable structure with long-range nanoscale polar order consisting of polar vortices that are intertwined in three dimensions. The process of creating this persistent structure, which we refer to as a supercrystal (S) phase, is possible with sub-picosecond optical pulse excitation with light above the bandgap.

By tuning of the dielectric constant parameter, phase-field modelling reproduces the observed supercrystal phase and associates its formation with the screening by optically generated free carriers at the interfaces. In addition, the model self-consistently predicts a thermal erase process in agreement with experiments.

Structural signs of optical phase conversion

The creation of the S phase from a phase mixture of FE and V phases is summarized in Fig. 1. The three-dimensional (3D) spatial depiction of the phases is extracted from a phenomenological phase-field model (see Methods), where the starting two-phase mixture in the as-grown heterostructure shown in Fig. 1a has been confirmed by a multitude of experimental observations on PTO/STO superlattices¹⁶. Using sub-picosecond optical pulses, these FE and V phases can be converted into the S phase (see Fig. 1a). These phases were experimentally mapped using X-ray scattering and structural imaging with area detectors (see Fig. 1b) to characterize the initial and photoinduced S phase in $n=16$ superlattices. The results show

¹Department of Materials Science and Engineering, Pennsylvania State University, University Park, PA, USA. ²Center for Nanophase Materials Sciences, Oak Ridge, TN, USA. ³Advanced Photon Source, Argonne National Laboratory, Argonne, IL, USA. ⁴Department of Materials Science and Engineering, University of California, Berkeley, CA, USA. ⁵Materials Sciences Division, Lawrence Berkeley National Laboratory, Berkeley, CA, USA.

*e-mail: vxg8@psu.edu; freeland@anl.gov

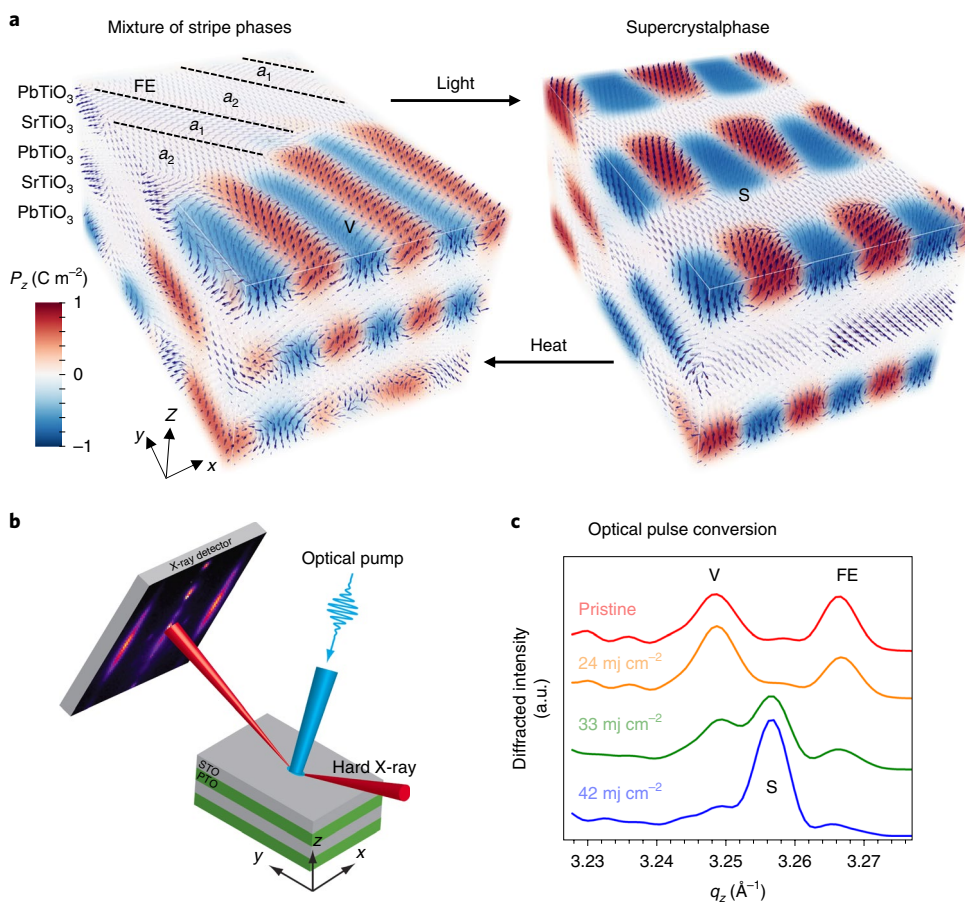


Fig. 1 | Summary of supercrystal formation. **a**, A two-phase mixture of in-plane ferroelectric-ferroelastic a_1/a_2 domains (FE) and polar vortex (V) is converted to a single 3D supercrystal (S) phase by sub-picosecond optical pulses in a PTO/STO superlattice. The S phase contains ferroelectric, ferroelastic and polar vortex sub-regions ordered in 3D. Thermal annealing reverses this transition. The arrows in **a** indicate the local polar displacements obtained from a phase-field model. The red and blue colour contrasts illustrate the up and down z -component of the polarization (P_z). The white regions correspond to in-plane polarization. **b**, The 400 nm wavelength optical-pump, X-ray diffraction probe study configuration. The real-space directions are aligned with reciprocal space and substrate crystallographic directions in the following way: $x \parallel H \parallel [001]$, $y \parallel K \parallel [-110]$ and $z \parallel L \parallel [110]$. **c**, Superlattice peaks near 002_{pc} (pseudocubic notation) showing two distinct diffraction peaks, corresponding to the V and FE phases in the pristine sample, that transform into a single uniform S phase with single-shot optical excitation above a certain threshold energy density. a.u., arbitrary units.

a collapse of the mixed phase, with two superlattice peaks corresponding to regions of FE and V that convert post-excitation to a single S-phase superlattice peak (see Fig. 1c). The coherent ordering of the S phase stems from its polar nature as well as the interaction with optical pulses, and represents a hidden order that is not present in the equilibrium phase diagram. Thermal annealing, however, can be used to erase the S phase and convert back to the starting two-phase mixture.

Next, we determine the detailed structure of the S phase using X-ray diffraction and microscopy. Figure 2a, b depicts the reciprocal space scans in the K - L reciprocal plane, corresponding to the y - z plane in real space, where the y and z axes are aligned with the $[-110]$ and $[110]$ directions of the DSO substrate, respectively. In the pristine state, the distinct out-of-plane lattice constant of the FE and V phases coexist to give rise to two independent superlattice reflections along the $[0\ 0\ L]$ direction¹⁶, as labelled in Fig. 2a. Upon optical excitation above a critical fluence using pulses shorter than 900 fs and 400 nm wavelength light, the two-phase mixture transforms into the S phase, possessing a long-range 3D coherent arrangement of polarization, strain and charge in an orthorhombic supercell size of approximately $11 \times 30 \times 25 \text{ nm}^3$. Accordingly, the two superlattice reflections of the pristine state collapse into a single vertical superlattice reflection (Fig. 2b), with the simultaneous

appearance of strong peaks in the off-specular part of the spectrum resulting from a fully coherent 3D modulation of the lattice with a well-defined periodicity of approximately $30 \text{ nm} \times 25 \text{ nm}$ in the y - z plane, respectively. The reciprocal space cuts along the H - K and H - L planes show this phase is fully 3D-ordered (Supplementary Figs. 1,2). Figure 2c,d shows the X-ray diffraction microscopy (XDM) map of the strain in the $(103)_{\text{pc}}$ lattice planes obtained from full-field Bragg imaging^{18,19}, which reveals that in their pristine FE+V state, the FE and V domains have a quasi-periodic stripe pattern with an approximately 350 nm periodicity in the plane of the PTO layer, which is in agreement with piezoresponse force microscopy (PFM) measurements¹⁶. A third periodicity of 11 nm, characteristic of the V ordering in the pristine samples¹⁴⁻¹⁶, also appears along the x direction (that is, the $[001]$ direction of the DSO substrate as shown in Supplementary Figs. 1,2).

After light irradiation, the FE and V phases are erased and a new uniform S phase is formed. In the S phase, the strong meso-scale strain modulations characteristic of the FE + V-phase mixture (Fig. 2c) are replaced by a uniform strain state (Fig. 2d) as probed by XDM. Note that the S-phase structural modulations occurring on a length scale of less than 30 nm are below the real space XDM resolution of 60 nm. Concomitant with the formation of a uniform strain state for the S phase, the structural coherency is greatly enhanced,

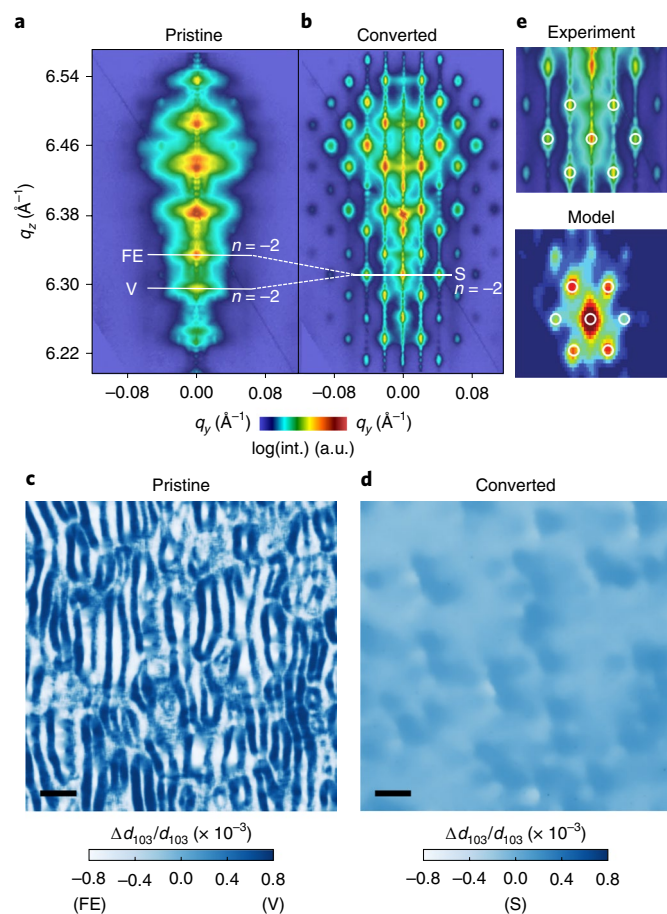


Fig. 2 | Supercrystal observation by X-ray diffraction and microscopy. **a**, Diffraction along the K - L (q_y - q_z) plane near the 004_{pc} peak for the mixed phase (FE + V) pristine sample shows evidence of order only along the z direction, with distinct peaks due to the FE and V phases, as noted by the horizontal lines. **b**, Upon optical excitation with light above the PTO bandgap, a periodic two-dimensional diffraction pattern appears due to spatial ordering in the y - z plane. **c**, Diffraction microscopy of the pristine phase shows a large mesoscale strain variation due to the mixture of FE (light) and V (dark) phases. **d**, With the formation of the supercrystal phase, the strain variation is strongly reduced and the image contrast becomes uniform on the mesoscale. The scale bars in **c** and **d** are 500 nm. **e**, The experimental diffraction pattern of the S phase (extracted from **b**) is in good agreement with a fast Fourier transform of the real-space structure from the phase-field model.

which can be seen by the formation of Laue fringes between superlattice and satellite peaks (Fig. 2b). In addition, the in-plane diffraction shows the formation of a strain state that is in direct registry with the substrate and persists throughout the entire superlattice (see Supplementary Fig. 3). This finding represents a highly unusual case where light irradiation of the sample greatly enhances the long-range strain coherency when it is assisted by spatially modulated polar displacements on the nanoscale. Second-harmonic generation and PFM measurements support that the S phase is polar (Supplementary Fig. 4). Attempts to resolve the atomic structure with high-resolution transmission electron microscopy (TEM) have not been successful to date due to the instability of the S phase during TEM specimen preparation.

Writing and erasing of the supercrystal state

To understand the formation process of the S phase, we explored in detail the characteristics of the response to the nature of

ultrafast excitation. The first observation is that it requires direct carrier excitation above the bandgap²⁰ of the PTO layer with 400 nm optical pulses, whereas excitations below the bandgap do not result in S-phase formation. Furthermore, the S-phase formation is obtained by optical-pulse irradiation only above a critical laser fluence (Fig. 3a). In addition, the laser fluence threshold was found to systematically increase with pulse duration (Fig. 3b). These results are consistent with a critical peak photo-carrier density for transformation that needs to be created before the photoinduced charge carriers can undergo relaxation.

Additional support for a non-equilibrium electronic process is shown in the temperature dependence of the S phase. Although we have seen that under ambient conditions the S phase is stable for at least a year, heating experiments show that the S phase is stable up to a temperature of ~ 430 K and disappears at a critical temperature of $T_s \approx 470$ K (Fig. 3c). After exceeding T_s , the sample exists in the pure FE phase and then returns to a mixture of FE + V phases upon cooling (Supplementary Figs. 5,6). Given this result, any ultrafast heating would serve only to destabilize the S phase and not create it. In addition, the write/erase process is entirely repeatable and the S phase has been successfully written and erased multiple times on several different samples, which suggests that it is unambiguously connected with intrinsic physical processes in the superlattice. For both the write and erase process, there is a sharp transition where ordering or disordering of the S phase occurs when a threshold value for the control parameter is reached.

Photoinduced phase formation and modelling

To study formation of the S phase, we consider first how these observations fit within the current understanding of polar heterostructures. Previous ultrafast optical-excitation studies of PTO nanolayers²¹ and superlattices²² have observed lattice dynamics due to optically generated carriers that segregate to the surface/interface and result in a reduction of the depolarizing field via charge-carrier screening, but no conversion to a polar state was observed. For the case of PTO/STO superlattices, an additional factor is the band-bending at the PTO/STO boundary^{23,24}, which can lead photo-induced carriers in STO to be trapped near the interface. It is known that photocarriers in STO cause a large increase in the dielectric constant²⁵ due to the formation of polarons²⁶, which are an additional source for screening the polar structure in PTO. From a view as a capacitor-like structure, where the strongly polar PTO is sandwiched between dielectric STO layers with smaller relative polarizability, modifications of the vertical depolarizing electric field, $E_d \sim CP_2/\epsilon_0\epsilon_{PTO}$ (refs. 27,28) can occur both from charge carrier screening, C , and changes in the relative dielectric permittivity, ϵ_{PTO} . For these reasons, in the modelling of the process we have focused on photocarrier-driven reduction of the depolarizing field as the primary modality.

To model the structure and creation of the S phase, we employ phase-field techniques²⁹, which have successfully predicted the coexistence of the pristine FE + V phase mixture¹⁴⁻¹⁶. Here, we focus on altering the depolarizing field by accounting for its reduction by photocarrier screening. In this phenomenological model, the tuning of the depolarizing field is achieved by modifying a single material parameter: namely, the background dielectric constant, ϵ_b (ref. 15). We note that the primary effect of changing ϵ_b is to mimic the charge-carrier screening of the local internal field while preserving the dielectric approximation of the phase-field models. In this way, the ϵ_b increase is assumed to incorporate possible contributions to the internal-field screening, such as ionized impurities and free- or trapped-charge carriers. As noted above, the two-phase pristine state has been well described using ϵ_b values of ~ 10 – 20 (refs. 15,16). By increasing ϵ_b , the energy for a polar displacement reorientation from in-plane to out-of-plane is reduced by generating bound charge accumulation at interfaces that compensates the local-polarization

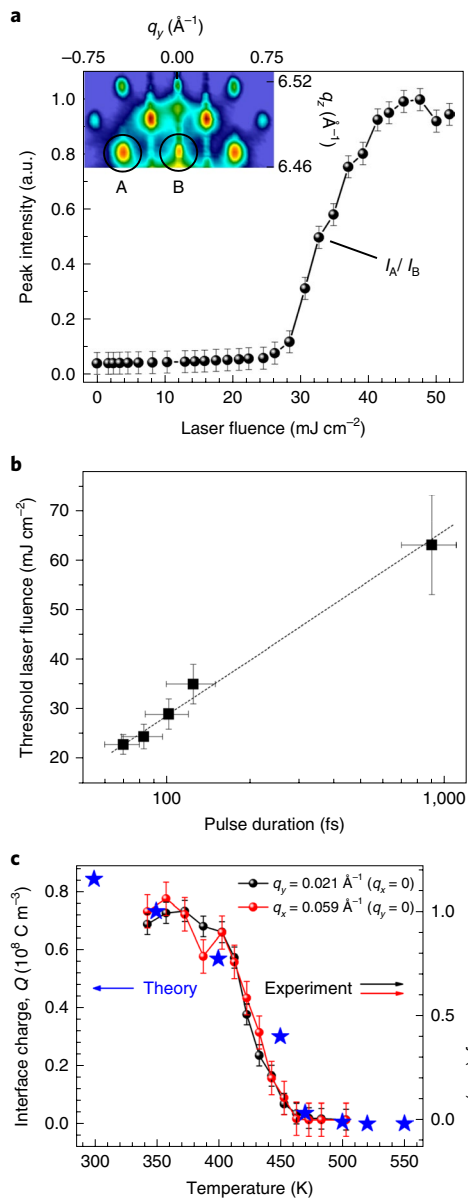


Fig. 3 | Reversible control of supercrystal phase formation. **a**, Laser fluence dependence of S-phase formation determined from the in-plane S-phase reflection (I_A) normalized to the specular peak (I_B) following a multi-shot exposure (~500 shots) to ~80 fs optical pulses, showing a critical fluence of ~25 mJ cm⁻². Inset is the corresponding K - L diffraction pattern near 004_{pc}. **b**, The variation of laser fluence threshold with pulse duration at 300 K extracted from normalized intensity changes of the in-plane ordering peak of the S phase, as shown in **a**. **c**, Right: temperature dependence of in-plane S-phase ordering peaks along the H and K directions (red and black dots), which shows stability near room temperature and the abrupt disappearance of the S phase at high temperature. Left: comparison with temperature-dependent calculations of the interfacial charge density from phase field modelling (blue stars). All error bars are determined from the standard deviation of fits to the data.

discontinuity. Moreover, above a critical value of $\epsilon_b \approx 80$, there is a clear discontinuity in the total energy at the point where the S phase emerges (Fig. 4a). In Fig. 4b, we have provided spatial maps of the vertical-polarization component showing how the system transitions from the mixed FE + V state into a single S phase at the critical value. During the S-phase transition, the electrical and gradient

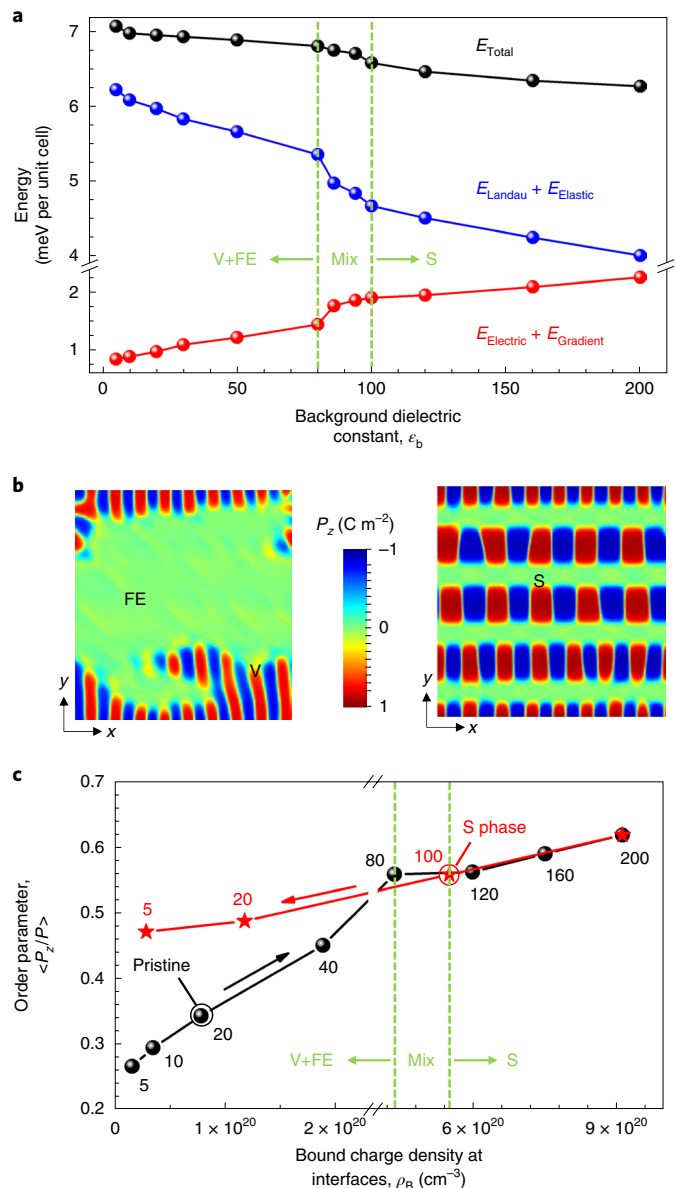


Fig. 4 | Phase-field model prediction of the supercrystal phase. **a**, Energy evolution versus background dielectric constant, ϵ_b , showing the evolution of the four terms in the free energy for $\epsilon_b < 80$, where energy increases for the electric and gradient energy are compensated by Landau and elastic contributions to the total energy. For ϵ_b between 80 and 100, all energy contributions change more abruptly, marking the transition to the S phase, followed by recovery of relatively slower changes at $\epsilon_b > 100$ after S-phase formation is completed. **b**, Vertical component of polarization spatial distributions at ϵ_b values below and above the threshold. **c**, Phase diagram showing the evolution of P_z inside a PTO layer plotted versus the bound charge density, ρ_B , at the interface between PTO and STO, which correlates with the background dielectric constant, ϵ_b (values noted on plot). On increasing ϵ_b , there is a transition from FE + V phase to S phase at a threshold $\epsilon_b = 80$ and the S phase remains for values above this level (black dots). The subsequent relaxation of ϵ_b back to lower values (red stars), shows the S-phase ordering remains quasi-stable even below the threshold value.

energies increase, but the reduction of the elastic and Landau energy contributions move the system towards a new energy minimum. A similar interplay in the S-phase formation energetics is observed

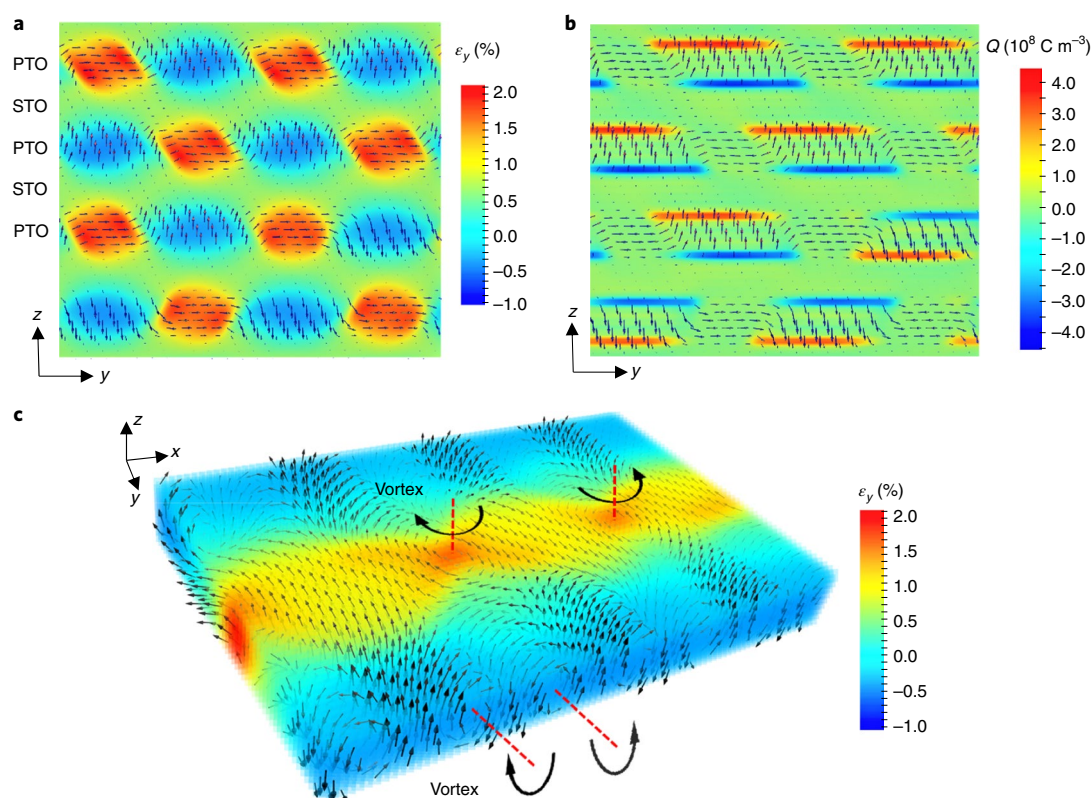


Fig. 5 | Interplay between order parameters within the supercrystal phase captured by the phase-field model. a,b, Spatially correlated ordering of an in-plane strain distribution (**a**) and the corresponding bound charge distribution (**b**) that are overlaid with polar displacement vector maps inside a selected y - z plane of the superlattice. The horizontally polarized regions from adjacent PTO layers interact elastically and electrically through the STO layer, which creates an antiphase stacking as the most stable configuration. **c.** A 3D view of a representative PTO layer, where the in-plane strain (ϵ_y) distribution is overlaid with polar displacement vector maps. Along the x - y plane, the polar vortex order alternates between in-plane and out-of-plane orientations for their respective vortex axes.

during the dynamic transition to the S phase following a sudden increase of ϵ_b from 5 to 200 (Supplementary Fig. 7). This nanoscale transformation of the polar order is characterized by an increase of the spatial average of the vertical-polarization component, P_z , which is correlated with the bound charge accumulated at interfaces and is quasi-linearly dependent on ϵ_b , as shown in Fig. 4c (see also Supplementary Fig. 8a). Furthermore, the gradual increase of ϵ_b is indeed reducing the depolarizing field at the superlattice interfaces as expected (see Supplementary Fig. 8b), which in turn allows the formation of structures with larger effective P_z . Accordingly, when $\epsilon_b < 80$, the increase of average vertical-polarization component evolves by an increase of the V phase volume fraction at the expense of the FE phase. There is a clear boundary for $\epsilon_b > 80$, where the FE phase collapses and the S phase is formed. To see how carrier relaxation would affect the S-phase stability after its formation, we also followed the phases formed as ϵ_b was decreased to the starting value below the phase conversion threshold and observed a significantly larger average P_z and the presence of a disordered S phase.

Strain, polarization and charge ordering

These results confirm the key role for optically induced dielectric changes in altering the overall energy landscape, which in turn allows the persistent formation of ordered states that are not accessible otherwise. To connect the values of ϵ_b to the experimental conditions, we use both the observed and calculated strain to assign a value of ϵ_b corresponding to experimental pristine and converted phases. The ϵ_b value that produces a strain state that matches the experimental observations is ~ 20 (bound charge density of $\sim 0.78 \times 10^{19} \text{ cm}^{-3}$) for the pristine state and ~ 100 (bound

charge density of $\sim 5.5 \times 10^{20} \text{ cm}^{-3}$) for the converted S-phase state, indicating a large enhancement for bound charge accumulation at interfaces.

To connect phase-field modelling with the observed structural modulations, we note that strong diffuse scattering is connected to the nanometre-scale lattice modulations that are created at the atomic level by the direction of the polar distortions. To mimic this effect from the polar lattice, as well as the charging of the structure, we further show the local polarization variation superimposed with the in-plane strain modulations throughout the 3D structure (Fig. 5a) along with a map of the bound charge distribution (Fig. 5b and Supplementary Fig. 9a). The formation of polar nanoregions within the S phase lead to lattice distortions in the y - z plane that match the symmetry of the X-ray diffraction by a fast Fourier transform of the model structure (Fig. 2e). Phase-field modelling is then seen to reproduce the observed structural symmetry of the S phase, suggesting a plausible mechanism for tuning the effect of the internal field by which such a phase can emerge. For the ordering in the plane of the sample (Fig. 5c and Supplementary Fig. 9b,c), we find arrays of intertwined polar vortices with both vertical and horizontal core axis orientations, in contrast to the V phase, which has vortex axes only in the plane of the PTO film layers. Further, unlike the V phase, which only has local correlations within a single domain and very weak correlations vertically between layers, the vortices in the S phase are ordered in 3D. From the temperature-dependent phase field results, the changes of the calculated bound charge density correlate well with the X-ray results (Fig. 3c). Overall, the observation of a dramatic phase transition from the FE+V to the S phase, which is optically induced in the experiments, shows

consistency with the model regarding the essential aspects: symmetry and periodicities (Fig. 2e), existence of a critical threshold for conversion (Figs. 3a and 4a), as well as an enhanced thermal stability (Supplementary Figs. 10–12).

Outlook

We note that microscopic mechanisms consisting of ultrafast carriers and lattice dynamics, ultimately underlying the supercrystal formation, are not accessible via our phenomenological modelling and must be addressed in future work. Nonetheless, good agreement between experiments and phase-field modelling, in particular in the latter's capability to reproduce the evolution of structural phases as a function of temperature without any additional parameter tuning (see Fig. 3c), gives strong support to a formation mechanism dominated by reduction of the depolarizing field via photocarrier excitation. In contrast to the photo-excitation of bulk crystals or crystalline thin films that show no new phases, the creation of a polar supercrystal with a sub-picosecond optical pulse highlights the special role of the superlattice geometry employed here, especially in the local spatial confinement of the ferroelectric order parameter. With photocarrier excitation occurring primarily in the PTO layer, the proximal unexcited 'cold' STO interlayers can act as nanoscale heat sinks to promptly spread out the competing thermal excitations, which may quench the optically stimulated transient states by exploiting non-adiabatic conditions to develop long-range order in a way that might not be accessible by equilibrium pathways. This understanding also highlights routes to stabilize these polar phases via tuning of the boundary conditions through alteration of the dielectric spacer material or environmental conditions.

Our discovery of this supercrystal formation reveals that the coupling between the superlattice layers can be optically manipulated to promote enhanced elastic interactions via optical pulse triggering of an electric perturbation. In turn, we can access a type of ordering that consists of interpenetrating polar vortices inside this long-range 3D-ordered structure with nanoscale periodicity. This phase captures and stores the light-activated carriers in a highly 3D charge-ordered state, which could be a potential strategy for charge storage and highly tunable capacitors. More broadly, the idea of counterpoising other competing magnetic, charge and orbital states into heterostructures and perturbing them with light or fields could trigger electronic, orbital and magnetically ordered supercrystals with novel structures and functionalities.

Online content

Any methods, additional references, Nature Research reporting summaries, source data, statements of data availability and associated accession codes are available at <https://doi.org/10.1038/s41563-019-0311-x>.

Received: 15 June 2018; Accepted: 4 February 2019;
Published online: 18 March 2019

References

- Basov, D., Averitt, R. D., van der Marel, D., Dressel, M. & Haule, K. Electrodynamic of correlated electron materials. *Rev. Mod. Phys.* **83**, 471–541 (2011).
- Zhang, J. & Averitt, R. D. Dynamics and control in complex transition metal oxides. *Annu. Rev. Mater. Res.* **44**, 19–43 (2014).
- Giannetti, C. et al. Ultrafast optical spectroscopy of strongly correlated materials and high-temperature superconductors: a non-equilibrium approach. *Adv. Phys.* **65**, 58–238 (2016).
- Kirilyuk, A., Kimel, A. V. & Rasing, T. Ultrafast optical manipulation of magnetic order. *Rev. Mod. Phys.* **82**, 2731–2784 (2010).
- Fausti, D. et al. Light-induced superconductivity in a stripe-ordered cuprate. *Science* **331**, 189–191 (2011).
- Torchinsky, D. H., Mahmood, F., Bollinger, A. T., Bozovic, I. & Gedik, N. Fluctuating charge-density waves in a cuprate superconductor. *Nat. Mater.* **12**, 387–391 (2013).
- Kim, K. W. et al. Ultrafast transient generation of spin-density-wave order in the normal state of BaFe₂As₂ driven by coherent lattice vibrations. *Nat. Mater.* **11**, 497–501 (2012).
- Wuttig, M. & Yamada, N. Phase-change materials for rewriteable data storage. *Nat. Mater.* **6**, 824–832 (2007).
- Ichikawa, H. et al. Transient photoinduced 'hidden' phase in a manganite. *Nat. Mater.* **10**, 101–105 (2011).
- Tao, Z. et al. The nature of photoinduced phase transition and metastable states in vanadium dioxide. *Sci. Rep.* **6**, 38514 (2016).
- Stojchevska, L. et al. Ultrafast switching to a stable hidden quantum state in an electronic crystal. *Science* **344**, 177–180 (2014).
- Zhang, J. et al. Cooperative photoinduced metastable phase control in strained manganite films. *Nat. Mater.* **15**, 956–960 (2016).
- Aguado-Puente, P. & Junquera, J. Structural and energetic properties of domains in PbTiO₃/SrTiO₃ superlattices from first principles. *Phys. Rev. B* **85**, 184105 (2012).
- Yadav, A. K. et al. Observation of polar vortices in oxide superlattices. *Nature* **530**, 198–201 (2016).
- Hong, Z. et al. Stability of polar vortex lattice in ferroelectric superlattices. *Nano Lett.* **17**, 2246–2252 (2017).
- Damodaran, A. R. et al. Phase coexistence and electric-field control of toroidal order in oxide superlattices. *Nat. Mater.* **16**, 1003–1009 (2017).
- Lu, L. et al. Topological defects with distinct dipole configurations in PbTiO₃-SrTiO₃ multilayer films. *Phys. Rev. Lett.* **12**, 177601 (2018).
- Laanait, N. et al. Full-field X-ray reflection microscopy of epitaxial thin-films. *J. Synchrotron Radiat.* **21**, 1252–1261 (2014).
- Laanait, N., Zhang, Z. & Schlepütz, C. M. Imaging nanoscale lattice variations by machine learning of X-ray diffraction microscopy data. *Nanotechnology* **27**, 374002 (2016).
- Zelezny, V. et al. The variation of PbTiO₃ bandgap at ferroelectric phase transition. *J. Phys.-Condens. Matter* **28**, 025501 (2016).
- Daranciang, D. et al. Ultrafast photovoltaic response in ferroelectric nanolayers. *Phys. Rev. Lett.* **108**, 087601 (2012).
- Ahn, Y. et al. Photoinduced domain pattern transformation in ferroelectric-dielectric superlattices. *Phys. Rev. Lett.* **119**, 057601 (2017).
- Schafraek, R., Li, S., Chen, F., Wu, W. & Klein, A. PbTiO₃/SrTiO₃ interface: Energy band alignment and its relation to the limits of Fermi level variation. *Phys. Rev. B* **84**, 045317 (2011).
- Torres-Pardo, A. et al. Spectroscopic mapping of local structural distortions in ferroelectric PbTiO₃/SrTiO₃ superlattices at the unit-cell scale. *Phys. Rev. B* **84**, 220102 (2011).
- Hasegawa, T., Mouri, S.-I., Yamada, Y. & Tanaka, K. Giant photo-induced dielectricity in SrTiO₃. *J. Phys. Soc. Jpn* **72**, 41–44 (2003).
- Nasu, K. Photogeneration of superparaelectric large polarons in dielectrics with soft anharmonic *T_{1u}* phonons. *Phys. Rev. B* **67**, 174111 (2003).
- Mehta, R. R., Silverman, B. D. & Jacobs, J. T. Depolarization fields in thin ferroelectric films. *J. Appl. Phys.* **44**, 3379–3385 (2003).
- Kim, D.-J. et al. Polarization relaxation induced by a depolarization field in ultrathin ferroelectric BaTiO₃ capacitors. *Phys. Rev. Lett.* **95**, 237602 (2005).
- Chen, L.-Q. Phase-field method of phase transitions/domain structures in ferroelectric thin films: A review. *J. Am. Ceram. Soc.* **91**, 1835–1844 (2008).

Acknowledgements

V.A.S., Y.Y., L.W.M., C.D., L.-Q.C., H.W., V.G. and J.W.F. acknowledge support from the US Department of Energy, Office of Science, Office of Basic Energy Sciences, under Award Number DE-SC-0012375 for the development of the materials and ultrafast experiments. Z.H., S.L. and G.A.S. acknowledge support from the National Science Foundation (DMR-1210588) and National Science Foundation Center for Nanoscale Science grant number DMR-1420620. L.-Q. C. also acknowledges support from NSF DMR-1744213. Use of the Advanced Photon Source was supported by the US Department of Energy, Office of Science, under contract no. DE-AC02-06CH11357. PFM data were collected at PSU, University of California, Berkeley, and at the Center for Nanophase Materials Sciences, a DOE Office of Science User Facility at ORNL. N.L. acknowledges support from the Eugene P. Wigner Fellowship at Oak Ridge National Laboratory (ORNL), a US Department of Energy (DOE) facility managed by UT-Battelle, LLC for US DOE Office of Science under contract no. DE-AC05-00OR22725. R.R. and L.W.M. acknowledge funding from the Gordon and Betty Moore Foundation's EPiQS Initiative, under grant GBMF5307. NL acknowledges use of the Compute and Data Environment for Science (CADES) at the Oak Ridge National Laboratory. V.A.S. would like to thank C.M. Schlepütz and J. Hammonds for their development of rsMap3D, valuable discussions with H. Zhou, S. Kalinin, Q. Li, Y. Ren, J. Tischler and D.D. Fong, and C.A. Kurtz for technical support.

Author contributions

V.A.S. conceived of the central concepts and designed the experiments. V.A.S., together with H.W., J.W.F., N.L., Y.Y., Z.Z., M.R.M., D.A.W., A.R.D., J.K. and X.Z., conducted the synchrotron-based X-ray diffraction studies. M.R.M., A.Y., S.D., R.R. and L.W.M.

synthesized the materials. C.D., Z.H. and L.-Q.C. conducted the phase-field modelling and analysis in collaboration with V.A.S. N.L., S.L., A.R.D. and V.A.S. conducted the scanning probe-based PFM measurements. Y.Y. and V.A.S. conducted the SHG measurements. G.A.S. measured TEM to confirm sample quality. V.A.S., V.G. and J.W.F. wrote the manuscript with contributions from all authors. All authors discussed the results and implications of the work, and read, edited and commented on the manuscript at all stages.

Competing interests

The authors declare no competing interests.

Additional information

Supplementary information is available for this paper at <https://doi.org/10.1038/s41563-019-0311-x>.

Reprints and permissions information is available at www.nature.com/reprints.

Correspondence and requests for materials should be addressed to V.G. or J.W.F.

Publisher's note: Springer Nature remains neutral with regard to jurisdictional claims in published maps and institutional affiliations.

This is a US government work and not under copyright protection in the US; foreign copyright protection may apply, 2019

Methods

Superlattice growth using RHEED-assisted pulsed laser deposition.

Superlattices of $(\text{PbTiO}_3)_n/(\text{SrTiO}_3)_n$ were synthesized using reflection high-energy electron diffraction (RHEED)-assisted pulsed laser deposition with a KrF excimer laser. A buffer layer of ~ 2 unit cells SrRuO_3 was deposited on the DyScO_3 (110) substrates at a temperature and oxygen pressure of 700°C and 50 mtorr, respectively. Layers of $(\text{PbTiO}_3)_n/(\text{SrTiO}_3)_n$ ($n = 16$ unit cells) were grown at 620°C and 100 mtorr oxygen pressure. The intensity oscillations of the RHEED pattern were recorded throughout the deposition to monitor the layer-by-layer growth mode. The unit $(\text{PbTiO}_3)_n/(\text{SrTiO}_3)_n$ was repeated until the superlattice was about 100 nm thick (eight repeats). For all materials, the laser fluence was $\sim 1.5\text{ J cm}^{-2}$, and the repetition rate was 10 Hz. After growth, the superlattices were cooled to room temperature in 50 torr of oxygen. The targets used for the deposition were a single-crystalline SrTiO_3 target, a polycrystalline SrRuO_3 target, and a polycrystalline $\text{Pb}_{1-x}\text{TiO}_3$ target. A lead-rich target is necessary to deposit stoichiometric PbTiO_3 .

Ultrafast laser set-up. Optical excitation of the superlattice was explored using femtosecond laser single pulses as well as pulse trains generated by a Ti:sapphire regenerative amplifier at 1 kHz. The duration of pulses, the total number of pulses, optical wavelength and laser fluence were all used for optical control of phase changes. The laser pulse duration was adjusted below 1 ps and measured using a single-shot autocorrelator. The laser wavelength was adjusted to be either 400 nm or 800 nm, with an excitation laser fluence below 50 mJ cm^{-2} to avoid damage. The use of optical pulses longer than ~ 1 ps has resulted in a spatially non-uniform phase conversion.

X-ray diffraction (XRD). XRD data were taken at the Advanced Photon Source using beamlines 7-ID-C, 11-ID-D, 33-BM and 33-ID-C using a Pilatus area detector. XRD data were converted into the reciprocal space representation using *rsMap3D* and cut along different directions to create different views of the data. The phase changes were monitored with XRD measurements of peaks and diffuse scattering satellites corresponding to in-plane periodic lattice modulations. Reciprocal lattice units from figures are in $2\pi/d_{\text{hkl}}\text{ \AA}^{-1}$, where d_{hkl} is the lattice spacing for the *hkl* reflection. Pseudocubic lattice parameters relative to the orthorhombic DyScO_3 substrate are shown in the following reference system: $[100]_{\text{pc}} \parallel [001]_{\text{o}}$ and $[010]_{\text{pc}} \parallel [-110]_{\text{o}}$.

XDM images were collected at the Advanced Photon Source using the XRIM instrument at beamline 33-ID-C at an energy of 10 keV and an effective real-space pixel size of 20 nm (XRIM instrumental specifications were reported previously¹⁸). XDM images were collected by scanning the (103) pseudocubic reflection of the PTO/STO superlattice along the (10L) truncation rod of the DyScO_3 substrate. Raw real-space XDM images were registered to the same sample location using feature extraction techniques as reported previously¹⁹. Extraction of the d_{103} spatial maps of the laser excited sample shown in Fig. 2d was performed using Gaussian Processes Regression, by fitting each spatially resolved *L*-scan. In the pristine sample, the presence of V and FE phase mixtures both laterally and along the superlattice thickness, with different d_{103} , lead to scattering contributions from both phases to the same pixel in the projected XDM image. We used a cross-correlation analysis between XDM images collected at the 01L peaks associated with the V and FE phases, respectively (Fig. 1c), to associate with each pixel in an XDM image a distinct phase, followed by the Gaussian Processes Regression technique to extract the d_{103} value for that pixel (as shown in Fig. 2c,d).

Phase-field simulations. For modelling of the polar structure change for the PTO/STO superlattice on a DSO substrate after the laser excitation, phase-field simulations are performed. The evolution of the order parameter (spontaneous polarization vector) is obtained by solving the time-dependent Ginzburg–Landau (TDGL) equations:

$$\frac{\partial P_i(\mathbf{r}, t)}{\partial t} = -L \frac{\delta F}{\delta P_i(\mathbf{r}, t)} \quad (i = 1, 2, 3) \quad (1)$$

where *L*, **r** and *t* denote the kinetic coefficient, spatial position vectors and evolution time step, respectively. The total free energy *F* can be expressed by the

volume integration of local Landau bulk, elastic/mechanical, electric/electrostatic and gradient energy densities, that is,

$$F = \int (f_{\text{Landau}} + f_{\text{elastic}} + f_{\text{electric}} + f_{\text{Gradient}}) dV \quad (2)$$

All the material constants for PbTiO_3 and SrTiO_3 used in the simulations are adopted from previous reports (see main text). A 3D phase-field simulation of PTO/STO superlattices is performed using discrete grids of $200 \times 200 \times 250$ with a grid spacing of 0.4 nm. The thicknesses of the substrate, film and air are set as 30, 176 and 44 grids, respectively. Periodic boundary conditions are applied in both the *x* and *y* directions, and a superposition method is used along the *z* direction. Random noise (with a magnitude of $< 0.00001\text{ C m}^{-2}$) is used as the initial set-up to simulate the thermal fluctuation during the annealing process. The mechanical boundary condition is applied such that the out-of-plane stress is fully released on the top of the film, while the out-of-plane displacement is zero on the bottom of the substrate sufficiently far away from the substrate/film interface. A short-circuit electric boundary condition is used where the electric potential at the top film surface and the film/substrate interface is fixed to zero. A mixed phase coexistence of a ferroelectric–ferroelastic a_1/a_2 -twin and polar vortex is first simulated as the initial structure (see main text) with the background dielectric constant set as 10. As shown in Fig. 1, the 3D structure is constructed by interconnecting of an a_1/a_2 -twin region with normal ferroelectric/ferroelastic twins and a vortex region with a continuous rotating polarization surrounding a vortex core. This structure is coherent with the experimental observations by PFM and TEM in the current PTO/STO system grown on a (110) DyScO_3 substrate at intermediate periodicities ($n = 10, 16$).

After the laser excitation, it is assumed that the superlattice film is more conducting due to photo-carrier excitation. As a consequence, the background dielectric constant for the superlattice is then increased to 200 to model the decrease of the internal depolarization field after the laser excitation. The 3D complex hierarchical ladder-like supercrystal phase is formed with periodical vortex arrays separating by *a*-domains (shown in Fig. 1), in good agreement with the experimental X-ray diffraction patterns.

Optical second-harmonic generation. To verify the ferroelectric nature as well as the symmetry of the light-induced super crystal, we performed optical second-harmonic generation (SHG) polarimetry analysis. Room-temperature *p/s*-polarized SHG responses at 400 nm from the super crystal were recorded as a function of the optical polarization direction of an 800 nm beam under normal incidence. The sample was oriented with the $[\bar{1}10]$ substrate direction along the lab *X* axis (horizontal) and the $[001]$ substrate direction along the lab *Y* axis (see Supplementary Fig. 4). The high-quality polarization-dependent SHG signal revealed the ferroelectric nature of the super crystal, which can be modelled with both 4mm and mm2 point group symmetry with the rotational axis in the sample plane (solid lines). Since the superlattice unit cell length scale (~ 20 nm) is much smaller than that of optical wavelength (400 and 800 nm), this large unit cell acts as an effective symmetry object for the SHG probe. Furthermore, the 4mm point group symmetry can be ruled out due to the in-plane 4-fold rotation operation being incompatible with the superlattice stacking structure. Therefore, SHG analysis revealed mm2 point group symmetry of the supercrystal structure, in support of the reciprocal space mapping observations of orthorhombic symmetry at the supercrystal cell level.

Topography and domain structure characterization. PFM and atomic force microscopy were performed at Pennsylvania State University (Bruker Icon I), at University of California, Berkeley (MFP-3D, Asylum Research), and at the Center for Nanophase Materials Sciences, Oak Ridge National Laboratory (Cypher, Asylum).

Data availability

Raw data from the Advanced Photon Source and phase field results are available upon reasonable request. The X-ray diffraction reciprocal space volumes generated with *rsMap3D* for figures both in the main text and supplementary information are available at <https://anl.box.com/s/mdjujuby4dqf122bb9a6vbev8qeuqbqf> together with Python notebooks for interacting with the datasets. For non-Python users, the data can be viewed with the ParaView application available at www.paraview.org.